applied sciences

MDPI

Article

Theoretical and Experimental Analysis of the Effect of Vaporization Heat on the Interaction between Laser and Biological Tissue

Yuru Cheng [1,2,†], Yu Shen [2,3,*,†], Yuxia Gao [1,*], Ya Wen [2], Ze Lv [2,4], Erpeng Wang [5], Mingli Wang [1], Shenjin Zhang [2,3], Yong Bo [2,3] and Qinjun Peng [2,3]

1 School of Science, Yanshan University, Qinhuangdao 066004, China; yurucheng@stumail.ysu.edu.cn (Y.C.); wml@ysu.edu.cn (M.W.)
2 Key Lab of Solid-State Laser, Technical Institute of Physics and Chemistry, Chinese Academy of Sciences, Beijing 100190, China; wenya@mail.ipc.ac.cn (Y.W.); lvze191@mails.ucas.ac.cn (Z.L.); zhangshenjin@163.com (S.Z.); boyong@mail.ipc.ac.cn (Y.B.); pengqinjun@mail.ipc.ac.cn (Q.P.)
3 Key Lab of Functional Crystal and Laser Technology, Technical Institute of Physics and Chemistry, Chinese Academy of Sciences, Beijing 100190, China
4 University of Chinese Academy of Sciences, Beijing 100190, China
5 Institute of Optical Physics and Engineering Technology, Qilu Zhongke, Jinan 250000, China; wangerpengs@163.com
* Correspondence: shenyu@mail.ipc.ac.cn (Y.S.); gaoyuxia@ysu.edu.cn (Y.G.)
† These authors contributed equally to this work.

Abstract: A theoretical model, based on the classical Pennes' bioheat theory, incorporating various boundary conditions, was established and compared to analyze the influence of the latent heat of vaporization via simulation. The aim was to elucidate the extent of its influence. The thermal damage rate, governed by the vaporization heat of biological tissue, is introduced as a key factor. Functional relationships between temperature and incident laser power, spatial position, and time are derived from the classical Pennes' bioheat equation. According to the theoretical model, numerical simulations and experimental validations are conducted using Comsol Multiphysics 6.0, considering the tissue latent heat of vaporization. The model incorporating the latent heat of vaporization proved more suitable for analyzing the interactions between laser and biological tissue, evident from the degree of fit between simulated and experimental data. The minimum deviations between theoretical and experimental observations were determined to be 2.43% and 5.11% in temperature and thermal damage, respectively. Furthermore, this model can be extended to facilitate the theoretical analysis of the impact of vaporization heat from different primary tissue components on laser-tissue interaction.

Keywords: bioheat transfer; laser ablation; diffusion approximation equation; thermal damage; biological tissue

check for updates

Citation: Cheng, Y.; Shen, Y.; Gao, Y.; Wen, Y.; Lv, Z.; Wang, E.; Wang, M.; Zhang, S.; Bo, Y.; Peng, Q. Theoretical and Experimental Analysis of the Effect of Vaporization Heat on the Interaction between Laser and Biological Tissue. *Appl. Sci.* **2024**, *14*, 4333. https://doi.org/10.3390/app14104333

Academic Editor: Herbert Schneckenburger

Received: 19 April 2024
Revised: 15 May 2024
Accepted: 16 May 2024
Published: 20 May 2024

Copyright: © 2024 by the authors. Licensee MDPI, Basel, Switzerland. This article is an open access article distributed under the terms and conditions of the Creative Commons Attribution (CC BY) license (https://creativecommons.org/licenses/by/4.0/).

1. Introduction

Pennes' bioheat transfer theory, based on Fourier's law of conduction, is a classical model used to describe the temperature distribution throughout tissue. It assumes that the thermal disturbance propagates with an infinite speed [1–3]. It is the most frequently used model to study bioheat transfer in tissue.

As early as 2007, Yang et al. [4,5] measured the water content and temperature increase during the ablation procedure. They modeled the loss of water content and latent heat of water into the bioheat equation as a changing specific heat. The simulated temperature has better agreement with the experimental data than with the original Pennes' bioheat equation. Cavagnaro et al. [6] studied the temperature increases induced by microwave thermal ablation and considered the factor of latent heat of water according to Yang's study. Their results agreed well with the experimental values for models including vaporization.

Ahad et al. [7] added the water content and the latent heat of water as a heat source based on Pennes' bioheat equation to analyze the sensitivity of independent variables on the optimal treatment conditions. It indicated high accuracy for estimating temperature. Pouya et al. [8] established a model to optimize the laser dosimetry for the ablation of pancreatic ductal adenocarcinoma tumors. Their computational model is based on Pennes' bioheat model, and the latent heat of water is added together with the water content as an extra heat source. Their predicted results showed a good trend-wise agreement with ex vivo porcine tissue at a relatively low laser energy level. Conversely, Alireza et al. [9] investigated a dual sequential wavelength laser for port-wine-stain treatment through computer models for light propagation and distribution integrated with the bioheat transfer equation. They presented a hybrid numerical model that combines the Monte Carlo with Pennes' bioheat equation. The water content and latent heat of water were not considered in the model. Similarly, scholars such as Wang et al. [10], Pankaj et al. [11], and Babak et al. [12] did not consider the latent heat of water or the water content in their models. Nevertheless, they still achieved good agreement between simulation and experimental values. Many scholars have explored temperature dynamics using a moving laser heat source [12–14], yielding significant findings that mitigate the thermal effects on sensitive tissues such as the eyes and brain. Additionally, there is ongoing research focusing on the impact of interstitial space within tissue, which represents a current direction in bioheat transfer studies [15–17]. Furthermore, some models have incorporated changes in structural mechanics, offering new simulation approaches to account for additional mechanical alterations during the process of bioheat transfer [7,18].

This study incorporates the latent heat of vaporization along with the percentage of thermal damage as a novel source representing tissue latent heat into the Pennes' bioheat equation. Compared with methods utilizing changes in water content in biological tissue, this approach based on the percentage of thermal damage exhibits lower error rates. In the former method, the curve of numerical fitting often exhibits large error when compared with experimental measurement data, and there is no unified calculation formula. These issues arise due to: (1) the varying trend of water content in different tissues with temperature, and (2) the functional relationship of tissue differing depending on its survival state. This integration aims to comprehensively compare the theoretical and experimental effects of temperature and thermal damage distribution, particularly under high laser power irradiation.

2. Materials and Methodology

Recently, Singh et al. [19] focused on evaluating the extent of tumor damage considering the tumor margins for irregular tumors, while sparing the healthy tissue. Their analysis shows that a thermal damage of 10 is achieved within the entire tumor region. Additionally, a thermal damage of 4–10 is attained beyond the tumor margins, ensuring adherence to the protocol which states that the volume of damaged healthy tissue should not exceed the tumor volume. Both the conditions (i.e., temperatures above 55 °C near tumor boundaries and less than 5% thermal damage to healthy tissue) are achieved for a 3 mm distance beyond the tumor periphery. Corresponding SAR values and exposure duration are reported to achieve the ablation of the considered tumor while minimizing the damage beyond 3 mm (margin) of the tumor boundary. In summary, the iterative computational experiments suggest that margins less than 5 mm are sufficient for the given patient-specific tumor and the typical clinical criterion that requires sacrificing the 10 mm of excessive healthy tissue fringes does not need to be met.

To predict the temperature behavior of the tissue, the porcine liver has been chosen as the material for this simulation model. A modified version of Pennes' bioheat model has been developed for this purpose [3,20]:

$$\rho c \frac{\partial T(\mathbf{r},z,t,P)}{\partial t} = \nabla \cdot [k \nabla T(\mathbf{r},z,t,P)] + Q_{laser}(\mathbf{r},z,t,P) + Q_{bio} + Q_H(\mathbf{r},z,t,P) \quad (1)$$

where ρ, c, and k represent the density, specific heat, and thermal conductivity of the tissue, respectively. T denotes the tissue temperature. Q_{laser}, defined as the irradiated laser power [20], is given by [21]:

$$Q_{laser}(\mathbf{r}, z, t) = \mu_a I(\mathbf{r}, z, t) \tag{2}$$

where μ_a represents the absorption coefficient and I denotes the photon distribution in the tissue.

The last term on the right-hand side in Equation (1) represents the energy of the tissue evaporation, denoted as Q_H,

$$Q_H = -\rho\alpha \cdot \frac{\partial P(\%)}{\partial t} \tag{3}$$

The symbol α denotes the latent heat of tissue, which is replaced by the latent heat of water. The parameter P (%) represents the percentage of necrotic tissue, serving as a descriptor of the damage incurred [22–24]:

$$P(\%) = [1 - \exp(-\Omega)] \cdot 100\% \tag{4}$$

where Ω is defined by the Arrhenius rate process model to analyze the thermal damage of the tissue:

$$\Omega = \int_0^t A \cdot \exp\left(-\frac{E_a}{RT(t)}\right) dt \tag{5}$$

where A is the frequency factor, E_a is the activation energy of the denaturation reaction, and R is the universal gas constant. Therefore, the energy of the tissue evaporation is given by:

$$Q_H(r, z, t, P) = -\rho\alpha \times \frac{\partial\left\{1-\exp\left[-\int_0^t A\cdot\exp\left(-\frac{E_a}{R\cdot T(r,z,t,P)}dt\right)\right]\right\}\cdot 100\%}{\partial t} \tag{6}$$

According to the theory of diffusion approximation, I comprises collimated part I_c and the diffuse part I_d [1,25]. The collimated intensity I_c is given by Beer's law [21]:

$$I_c(\mathbf{r}, z, t) = I_0 \exp\left(-2\frac{r^2}{w_0^2}\right) \exp(-\mu_t' \cdot z) \cdot round\left[0.1321 + \exp\left(-\frac{t}{\tau}\right)\right] \tag{7}$$

where I_0 represents the initial laser intensity at the surface, w_0 denotes the radius of the laser beam on the surface, and $\mu_t{}' = \mu_a + \mu_s{}'$ stands for the effective attenuation coefficient, with μ_a being the absorption coefficient. $\mu_s{}' = \mu_s\,(1 - g)$ represents the effective scattering coefficient, where g signifies the anisotropy factor, and μ_s represents the scattering coefficient.

The diffuse part I_d is calculated by the diffusion approximation equation [26]:

$$\begin{cases} \frac{1}{v}\frac{\partial}{\partial t} I_d(\boldsymbol{r}, t) - D\nabla^2 I_d(\boldsymbol{r}, t) = -\mu_a I_d(\boldsymbol{r}, t) + \mu_s' I_c \\ I_c(\mathbf{r}, z) = (1 - R_0) \cdot I_0 \exp(-\mu_t' z) \exp\left[-\frac{2}{w_0^2} r^2\right] \end{cases} \tag{8}$$

where v represents the velocity of light in the medium, while $D = 1/3(\mu_a + \mu_s{}')$ denotes the diffusion coefficient. Additionally, R_0 signifies the light reflection at the tissue surface.

The parameters of the liver are detailed in Table 1.

The parameters pertaining to thermal damage, as defined by the Arrhenius rate process model, are presented in Table 2.

In both of these distinct conditions, the two-dimensional axisymmetric domain is partitioned into two regions comprising triangular elements. The geometric model, designated as areas 1 and 2, exhibits variations in size within the computational platform of Comsol Multiphysics 6.0. The mesh schematic and boundary conditions are illustrated in Figure 1. For area 1, characterized by a thickness of 10 mm and a radius of 2 mm. The maximum cell size measures 0.6 mm, while the minimum cell size is 2.25 μm. The

maximum unit growth rate stands at 1.2, with a curvature factor of 0.25. Conversely, in area 2, representing the entire tissue volume, the dimensions entail a thickness of 30 mm and a radius of 15 mm. Here, the maximum cell size is 1.11 mm, with a minimum cell size of 3.75 µm. The maximum unit growth rate remains consistent at 1.2, alongside a curvature factor of 0.25.

Table 1. Thermophysical and optical parameters of the liver.

Parameter	Symbol	Value	Ref.
Density	ρ	1050 kg/m^3	[16,27,28]
Specific heat	c	3770 J/(kg·K)	
Thermal conductivity	k	0.49 W/(m·K)	
Absorption coefficient	μ_a	0.064 mm^{-1}	[16,27,28]
Scattering coefficient	μ_s	4.72 mm^{-1}	
Refractive index	n	1.379	
Anisotropy factor	g	0.97	[29]

Table 2. Parameters of thermal damage.

Parameter	Symbol	Value	Ref.
Activation energy of the denaturation reaction	A	7.39×10^{39} s^{-1}	[30,31]
Frequency factor	E_a	2.577×10^5 J/mol	
Universal gas constant	R	8.3413 J/(mol·K)	

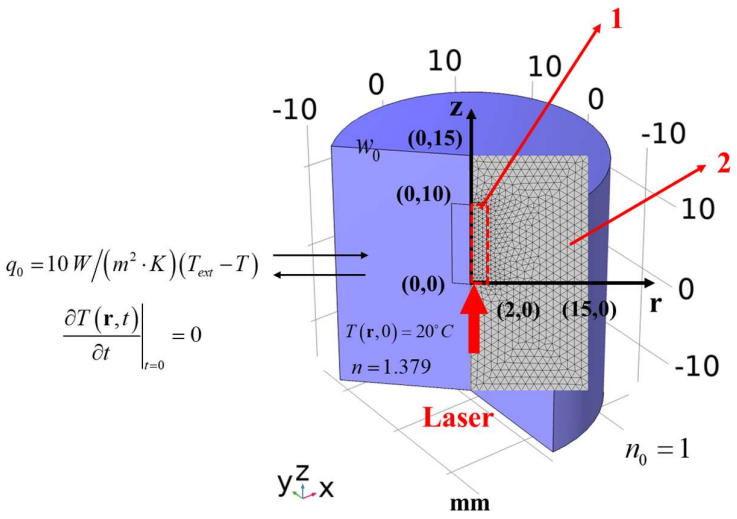


Figure 1. Mesh schematic and the boundary conditions of the liver in two-dimensional axisymmetric domain. Area 1 and area 2 represent two different mesh sizes, respectively.

3. Experimental Methods

The schematic diagram of the laser ablation experiment was drawn using Figdraw (https://www.figdraw.com/#/, accessed on 12 May 2024) and is depicted in Figure 2.

In this experimental setup, laser irradiation persists for a duration of 10 s in each experimental group, with the initial temperature set to 20 °C. A puncture needle is inserted directly into the sample to a depth of 2.5 cm. Thermocouples are strategically positioned at four locations along the laser irradiation direction, with their readings meticulously recorded by the digital display, as depicted in Figure 3. Initially, when the laser power is relatively low, signifying a shorter length of thermal damage, the first thermocouple is situated at z = 1 mm along the laser irradiation direction. The spacing between each thermocouple is maintained at 1 mm. Subsequently, as the power increases, the position of the first thermocouple gradually shifts farther away from the laser source. Consequently,

the spacing between each thermocouple is expanded to 2 mm. The total recording duration captured by the digital display spans 50 s.

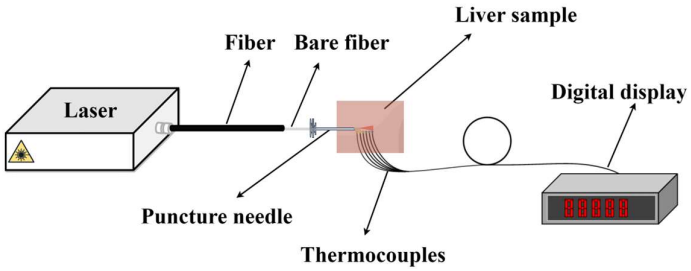


Figure 2. The schematic diagram of the laser ablation experiment.

The continuous wave (CW) LD laser (980 nm) utilized in the experiment is home-built, boasting a maximum power (*P*) capacity of up to 300 W. Energy transmission is facilitated by fibers with a core diameter of 800 µm. A puncture needle with an internal diameter of 1.8 mm and a length of 90 mm serves to guide the bare fiber to the targeted irradiation area. Fresh liver samples, procured from the slaughterhouse within a timeframe of less than 3 h, are utilized for the experiment. Temperature measurements along the axial direction are conducted using thermocouples (WRNK-191, Taizhou Suou electric heating appliance Co., Ltd., Taizhou, China) with a diameter of 1 mm, offering an accuracy of ±1.5 °C and a response speed of 0.5 s. The digital display (XSR40-V0) boasts an accuracy of ±0.2% F.S.

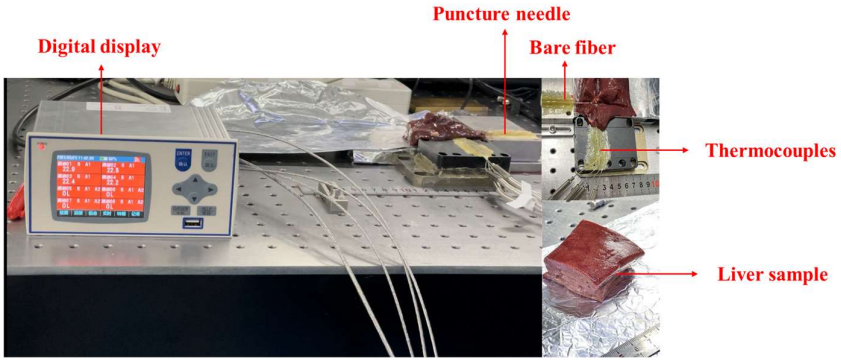


Figure 3. The ex vivo experimental setup for temperature measurement.

4. Results

4.1. Analysis of Temperature Distribution

The two-dimensional temperature distribution for varying laser powers with α = 0 kJ/kg and α = 2260 kJ/kg conditions, depicting temperatures exceeding 60 °C, is illustrated in Figure 4. As the laser power increases under both conditions, there is a corresponding rise in peak temperature and an expansion in the range of temperatures exceeding 60 °C. However, compared to the scenario without the addition of latent heat (α = 0 kJ/kg), incorporating the latent heat of water (α) results in lower peak temperatures and a narrower range of temperatures exceeding 60 °C. Further insights into temperature distribution are provided in Figure 5, detailing the volumes of temperatures exceeding 60 °C for each model. Notably, the volume difference is up to 232 times greater in the model with α = 0 kJ/kg compared to the model with α = 2260 kJ/kg at a laser power of 10 W.

The peak temperatures corresponding to different laser powers under both experimental conditions and simulations are depicted in Figure 6. It is assumed that the temperatures measured by the thermocouples represent the tissue temperature, indicating that the tissue does not undergo transformation into a gasified cavity. The experimental results align well with the α = 0 kJ/kg model, suggesting good agreement. However, it should be noted that tissue melting and vaporization into a gasified cavity occur when the temperature exceeds

600–700 °C, known as the threshold temperature [29]. Thus, it is imperative for the tissue temperature to remain below this threshold during laser irradiation to prevent gasification. The measured temperature surpasses the threshold temperature, possibly due to the direct absorption of photons by the thermocouples from the laser.

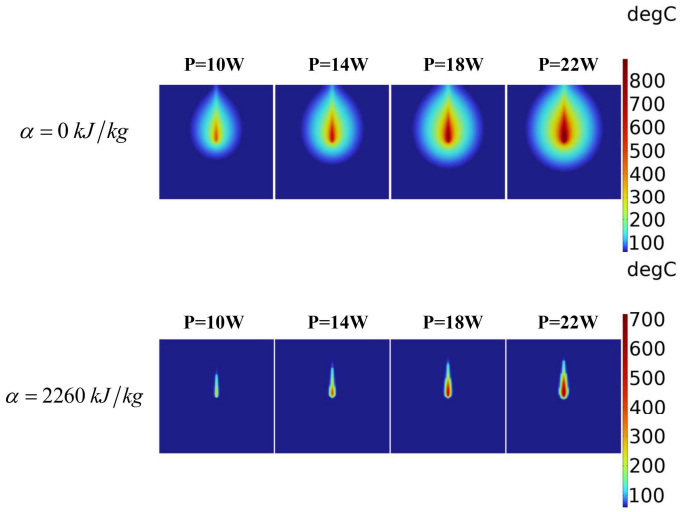


Figure 4. The two-dimensional temperature distribution depicting temperatures exceeding 60 °C under varying laser powers for two distinct conditions.

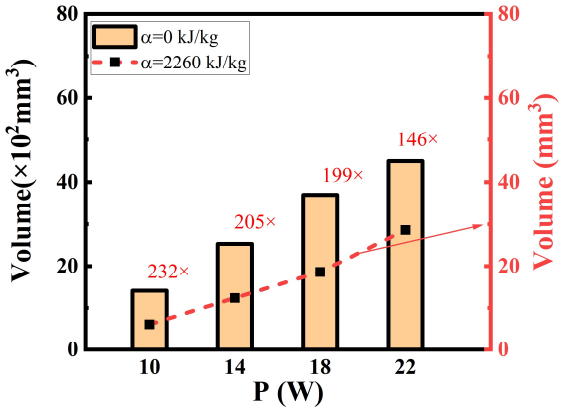


Figure 5. The volume of temperatures exceeding 60 °C under different laser power settings at t = 10 s for two distinct conditions.

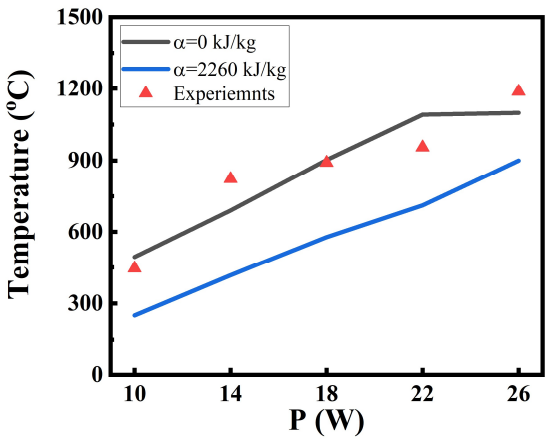


Figure 6. The peak temperatures corresponding to different laser powers.

This disparity can be attributed to the variability in the positioning of the fiber relative to the thermocouple during the experiment, deviating from the intended fixed configuration. Additionally, the soft texture of pork liver, coupled with its numerous blood vessels, poses a challenge for the accurate placement of the thermocouples at the desired temperature measurement points. The initial experimental temperature point was notably higher than the corresponding simulated results for each irradiated laser power. It is plausible to speculate that the positioning of the first thermocouple is closer to the laser ablation area, increasing the likelihood of absorbing photon energy directly from the laser irradiation. Therefore, any measured temperature exceeding 600–700 °C is considered invalid experimental data in this study.

The temperature distribution is thoroughly analyzed along the axial direction for the two conditions, α = 0 kJ/kg and α = 2260 kJ/kg, both theoretically and experimentally, as depicted in Figure 7. The model with α = 2260 kJ/kg exhibits a better fit with the experimental data compared to the model with α = 0 kJ/kg. Specifically, for a laser power of 10 W, the maximum deviation is 72.9% at z = 7 mm, while the minimum deviation is 2.43% at z = 1 mm. With a laser power of 14 W, the maximum deviation increases to 82% at z = 7 mm, with a minimum deviation of 10.4% at z = 1 mm. Similarly, for laser powers of 18 W and 22 W, the maximum deviations are 67.3% and 37.2% at z = 7 mm and z = 8 mm, respectively, with corresponding minimum deviations of 9.4% at z = 5 mm and 3.5% at z = 4 mm. In contrast, for the α = 0 kJ/kg model, the minimum deviation exceeds 40%, and the maximum deviation reaches up to 500%. Hence, the model with α = 2260 kJ/kg proves to be more suitable for analyzing the temperature distribution during the interaction between the laser and the tissue.

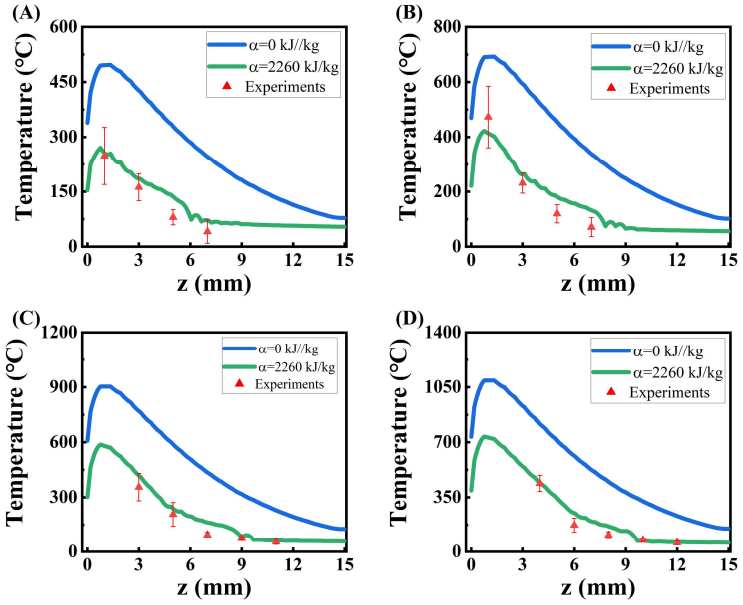


Figure 7. Temperature distribution along the axial direction, obtained from simulation data under two distinct conditions and experimental measurements. (**A**–**D**) P = 10 W, 14 W, 18 W, and 22 W.

The temperature distribution at various time points, particularly when the duration reaches 10 s, is illustrated in Figure 8. Notably, as the laser continues to irradiate points (0,1) and (0,3) with power levels of 10 W and 14 W, the temperature exhibits a noticeable rise, as depicted in Figure 8. A detailed comparison and discussion of the observed differences are provided. The experimental results align closely with the model employing α = 2260 kJ/kg, in contrast to the α = 0 kJ/kg model. At t = 10 s, the maximum temperature is recorded at 506 °C and 256 °C for the α = 0 kJ/kg and α = 2260 kJ/kg models, respectively. It was observed that the temperature rises rapidly initially, followed by a gradual slowdown until reaching its peak upon the cessation of laser irradiation, particularly evident in the α = 0 kJ/kg model. Furthermore, the temperature rise process exhibits greater fluctuation

for the α = 2260 kJ/kg model compared to the α = 0 kJ/kg model. The maximum deviation is observed to be 37.8% at t = 13 s, with a minimum deviation of 3.4% at t = 50 s for the point (0,1). Similarly, for the point (0,3), the maximum deviation is 24.1% at t = 14 s, with a minimum deviation of 4.9% at t = 10 s. The discrepancy in curve shape can be attributed to the varying states of aggregation of water, upon which α is based, influencing the energy absorption dynamics.

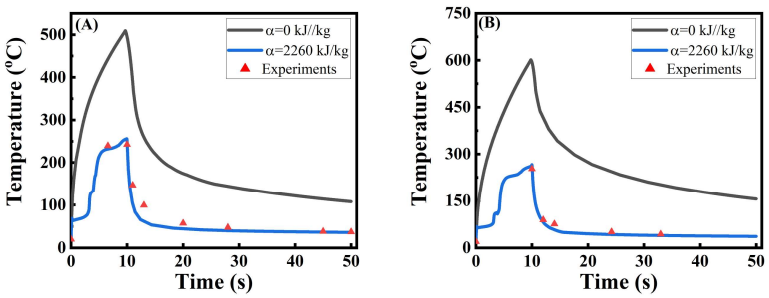


Figure 8. Temperature distribution at various time points when the duration reaches 10 s. (**A**) The laser power P = 10 W at point (0,1); (**B**) the laser power P = 14 W at point (0,3).

4.2. Analysis of Thermal Damage Distribution

A comprehensive analysis and comparison of thermal damage, both theoretically and experimentally, across different laser powers, are presented in this study. Significant disparities can be observed between the thermal damage profiles predicted by the two distinct conditions, as depicted in Figure 9. Moreover, the total volume of tissue damage, as illustrated in Figure 10, reveals substantial discrepancies between the models with α = 0 kJ/kg and α = 2260 kJ/kg. Specifically, the volume of damaged tissue is notably larger in the α = 0 kJ/kg model compared to the α = 2260 kJ/kg model, with the maximum magnification reaching 360 times at a laser power of 10 W. Furthermore, as shown in Figure 9, the extent of the thermal damage in the α = 0 kJ/kg model extends beyond the boundaries of the model. This renders it unsuitable for accurately estimating the thermal damage length, given the significantly higher simulation error compared to that observed experimentally.

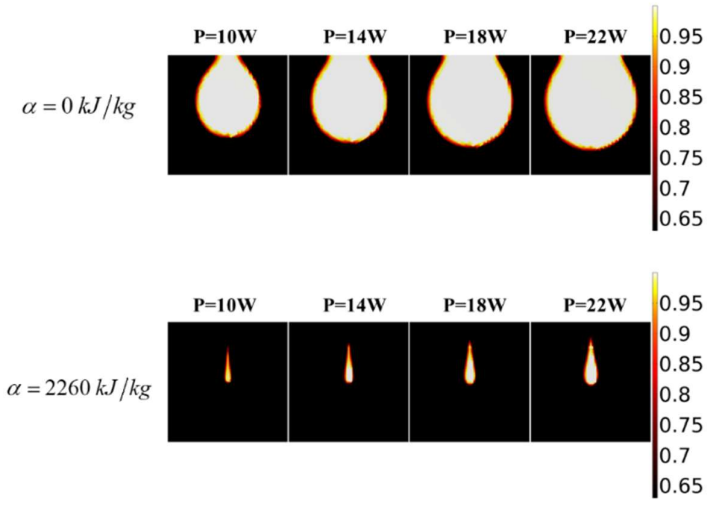


Figure 9. The two-dimensional thermal damage distribution under varying laser powers for two distinct conditions.

The thermal damage length between the condition of α = 0 kJ/kg and experimental values under different laser powers along the axial direction is illustrated in Figure 11. A high level of agreement was observed between the α = 2260 kJ/kg condition and the experimental data. In comparison to the experimental damage length, the minimum deviation is 5.11% with an average experimental length l = 4.28 mm at P = 10 W. Meanwhile,

the maximum deviation is 18.38% with an average experimental length of l = 7.55 mm at P = 18 W. Thus, the α = 2260 kJ/kg model was proven highly suitable for analyzing the thermal damage distribution during the interaction between the laser and the tissue.

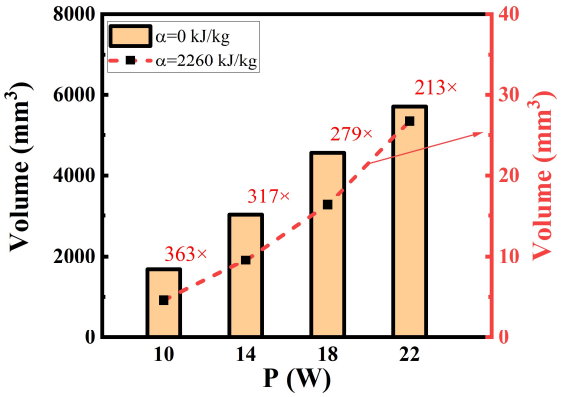


Figure 10. The volume of totally damaged tissue.

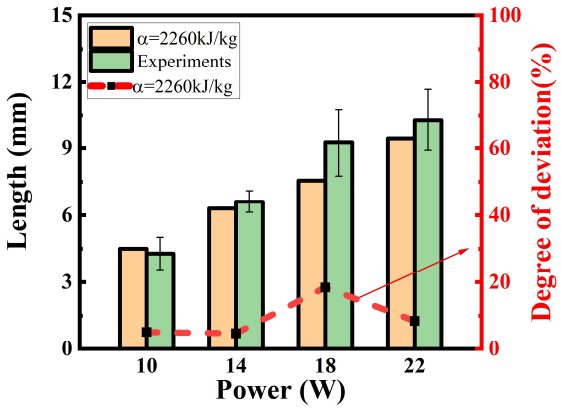


Figure 11. The thermal damage length and deviation between two distinct conditions with different laser power.

At least three valid experimental data points were selected. During the experiment, sources of error include instrument response time, sensitivity, the presence of large blood vessels or fascia tissue in the isolated pig liver, and other factors. These data points were subsequently averaged to compute the final mean square error. The resulting average uncertainty was determined to be ±49.3 °C for the temperature experiment and ±1.0 mm for the length of laser ablation.

5. Discussion

According to Singh's study, cellular and biological tissue heating may result in reversible (or repairable injury) and irreversible (or lethal) thermal cell-death in living biological tissue. The continuous regeneration of living human tissue due to the continuous supply of oxygen through arterial blood must be taken into account to counterbalance the thermal degradation at quasi-static thermal conditions. There is a regeneration of healthy cells at the interface of tumor-healthy tissue. At the interface, the regeneration of healthy cells triggers an immune response of biological tissue towards continued heating to suppress prevent and restrict the further accumulation of thermal damage within damage bounds of $\Omega \leq 1$. When modeling the kinetics of thermal damage to tumors, it is essential to incorporate the partial self-regeneration of normal connecting human tissues at the tumor periphery. This regeneration occurs due to the continuous matching of oxygen demands in the healthy tissue by the arterial blood [32]. Recent studies suggest a change in the interstitial space (porosity) of tissue during thermal ablation. In a systemic delivery of

nanoparticles to tumors, nanoparticles traverse through the pores in the tumor capillary walls and diffuse within the interstitial fluid space. If the initial diffusion distance (D_n) is 10 μm, the enhancement in D_n due to local heating could reach up to 23 μm. This enhancement holds significant potential for improving nanoparticle penetration in the interstitial space, given that the typical capillary-to-capillary distance in tumors ranges from approximately 50–100 μm. Therefore, employing mild or modest hyperthermia using magnetic nanoparticles as therapeutic agent carriers can achieve dual treatment efficacies by inducing thermal damage and enhancing uniform drug delivery [17]. In this theoretical model, ex vivo liver tissue is used as the sample, and factors such as blood flow and metabolic activity are not considered. Consequently, the contribution of oxygen from arterial blood can be disregarded in this simulation. Singh introduces a groundbreaking approach to modeling thermal processes in biological tissues by refining the classical Pennes' Bioheat Equation (3). By incorporating the concept of heterogeneous blood perfusion, the study offers a fresh perspective on heat transfer dynamics within living organisms. This novel modification allows for a more accurate representation of blood flow variations across different regions of the body, thereby enhancing the precision of thermal simulations in biomedical applications such as the laser-tissue interactions discussed in this work. Through rigorous mathematical analysis and numerical simulations, Singh demonstrates the efficacy of the proposed bioheat model in capturing the complexities of heat distribution and dissipation in heterogeneous tissue environments. This innovative research opens new avenues for exploring the intricacies of thermal physiology and holds significant promise for advancing the development of thermal therapies, biomedical device design, and clinical treatment planning. Through the accurate modeling of heat-source/heat sink, hot spots and cold-spots can be minimized. Areas with high blood perfusion tend to dissipate heat more rapidly, potentially leading to under-treatment, whereas regions with low perfusion may accumulate excessive heat, increasing the risk of over-treatment and collateral damage to nearby structures. By accounting for heterogeneous blood perfusion in thermal ablation models, clinicians can more accurately predict and control the distribution of thermal energy, thereby optimizing treatment efficacy and reducing the likelihood of adverse effects. Therefore, understanding and accounting for heterogeneous blood perfusion are critical considerations in thermal ablation procedures to ensure safe and successful outcomes for patients. We aim to address this novel development in upcoming work.

In a recent study, Zhu and colleagues proposed a temperature-dependent time delay at 43 °C [33]. Their findings suggest that the heating time required was at least 24% shorter than that predicted using the traditional Arrhenius integral, despite the initial time delay. Their conclusions emphasized the importance of integrating dynamic nanoparticle spreading during heating and an accurate thermal damage model into theoretical simulations of temperature elevations in tumors. This integration is crucial for determining the thermal dosage necessary for magnetic nanoparticle hyperthermia design. In contrast to the study by Zhu et al., this investigation utilizes the traditional Arrhenius model to simulate thermal damage distribution. Both in simulation and experimental setups, the photon count of the laser approximates 10^{20}, representing a substantial heat source.

Consequently, the tissue experiences rapid temperature escalation, swiftly reaching the threshold temperature and resulting in tissue vaporization. Gasification encompasses the most extensive area within our thermal damage models. Hence, a time delay is not accounted for in this investigation.

The overall algorithm was implemented using COMSOL Multiphysics 6.0, by establishing the two-dimensional axisymmetric domain mesh of liver. MUMPS (Multifrontal Massively Parallel sparse direct Solver) is used as the linear solver, with a default preordering algorithm used for solving the temperature and thermal fields. The tolerance factor is set to 1. The backward difference formula is used for time matching. The following nonlinear methods are highly nonlinear Newton methods, and the termination technique is iteration or tolerance, the number of iterations is 50, and the tolerance factor is 1.

Two distinct condition models, based on the classical Pennes' bioheat equation, were established and compared to analyze the influence of the latent heat of vaporization on simulation results. First, temperature distribution and thermal damage are investigated both theoretically and experimentally for the two conditions. The discrepancies and underlying reasons are thoroughly examined. The difference in the volume of temperatures exceeding 60 °C is up to 232 times greater in the α = 0 kJ/kg model compared to the α = 2260 kJ/kg model with a laser power of P = 10 W. For P = 10 W, the maximum deviation is 72.9% at z = 7 mm, while the minimum deviation is 2.43% at z = 1 mm. Similarly, for P = 14 W, the maximum deviation reaches 82% at z = 7 mm, with a minimum deviation of 10.4% at z = 1 mm. The trend continues, with deviations of 67.3% at z = 7 mm for P = 18 W and 37.2% at z = 8 mm for P = 22 W. Conversely, for the α = 0 kJ/kg model, deviations exceed 40% at their minimum and reach up to 500% at their maximum. When compared to experimental damage lengths, deviations range from 5.11% with an average experimental length of l = 4.28 mm at P = 10 W to 18.38% with an average experimental length of l = 7.55 mm at P = 18 W.

The model incorporating the latent heat of vaporization proved to be more appropriate for analyzing the interaction between the laser and biological tissue, as evidenced by the better fit between simulated and experimental data. Detailed theoretical analyses of both conditions were conducted, offering insights into the extent of α's influence on temperature and thermal damage distribution in the simulation results.

Moreover, this study presents a method that can be expanded to facilitate a theoretical analysis of the impact of the vaporization heat from various primary tissue components on the interaction between the laser and tissue. If it is feasible to acquire the enthalpy change corresponding to the primary substance in the tissue, based on the studies establishing a simple model connecting normalized enthalpy and the latent heat of vaporization [34,35], the new latent heat of the tissue can be calculated using the normalized enthalpy and the concentration of the main substance. The enthalpy change values of proteins can be measured using thermal analysis techniques such as differential scanning calorimetry (DSC) or isothermal calorimetry (ITC). These techniques measure the heat capacity of a protein at different temperatures to derive enthalpy change values. In addition, computational methods such as molecular dynamics simulations or quantum chemistry calculations can be used to estimate the enthalpy change of a protein. However, it is important to note that proteins are complex biological macromolecules, and their enthalpy change value can be influenced by many factors. As a result, measuring or estimating their enthalpy change value can present challenges. Considering the normalized enthalpy and change in interstitial space (porosity) of tissue during thermal ablation would be very helpful for improving the simulation accuracy.

Author Contributions: Conceptualization, Y.C. and Y.S.; methodology, Y.C.; software, Y.C.; validation, Y.C.; formal analysis, Y.C., Y.S. and Y.G.; investigation, Y.C. and Y.S.; resources, Y.C., Y.S. and Y.G.; data curation, Y.C. and Y.W.; writing—original draft preparation, Y.C.; writing—review and editing, Y.C., Y.S. and Y.G.; visualization, Y.C., Z.L. and E.W.; supervision, Y.S., Y.G., M.W., S.Z., Y.B. and Q.P.; project administration, Y.S. and Y.B.; funding acquisition, Y.S. All authors have read and agreed to the published version of the manuscript.

Funding: This research was funded by Global Common Challenges Project of International Partnership Program of Chinese Academy of Sciences (174GJHZ2022016GC); National Key Research and Development Program of China (key special projects, Young Scientist) (No. 2022YFB3607900); The National Special Support Program for high-level Talents Science and Technology (Innovation leading talent program Defense Technology Innovation Foundation) (No. SQ2022RA24910010); Technical Institute of Physics and Chemistry of the Chinese Academy of Sciences; Key Laboratory Foundation of Chinese Academy of Sciences, Key Lab of Solid State Laser (No. CXJJ-22S020); Talent introduction training program of Institute of Optical Physics and Engineering Technology, Qilu Zhongke (No. RK-JS-THZJG-22-01).

Institutional Review Board Statement: Not applicable.

Informed Consent Statement: Not applicable.

Data Availability Statement: The data that support the findings of this study are available from the corresponding author upon reasonable request. The data are not publicly available due to privacy.

Conflicts of Interest: The authors declare no conflicts of interest.

References

1. Jasiński, M.; Majchrzak, E.; Turchan, L. Numerical analysis of the interactions between laser and soft tissues using generalized dual-phase lag equation. *Appl. Math. Model.* **2016**, *40*, 750–762. [CrossRef]
2. Ziaei, P.; Moosavi, H.; Moradi, A. Analysis of the dual phase lag bio-heat transfer equation with constant and time-dependent heat flux constant on skin surface. *Therm. Sci.* **2016**, *20*, 1457–1472. [CrossRef]
3. Singh, M. Modified Pennes bioheat equation with heterogeneous blood perfusion: A newer perspective. *Int. J. Heat Mass Transf.* **2024**, *218*, 124698. [CrossRef]
4. Yang, D.; Converse, M.C.; Mahvi, D.M.; Webster, J.G. Measurement and Analysis of Tissue Temperature During Microwave Liver Ablation. *IEEE Trans. Biomed. Eng.* **2007**, *54*, 150–155. [CrossRef] [PubMed]
5. Yang, D.; Converse, M.C.; Mahvi, D.M.; Webster, J.G. Expanding the Bioheat Equation to Include Tissue Internal Water Evaporation During Heating. *IEEE Trans. Biomed. Eng.* **2007**, *54*, 1382–1388. [CrossRef] [PubMed]
6. Cavagnaro, M.; Pinto, R.; Lopresto, V. Numerical models to evaluate the temperature increase induced by ex vivo microwave thermal ablation. *Phys. Med. Biol.* **2015**, *60*, 3287–3311. [CrossRef] [PubMed]
7. Mohammadi, A.; Bianchi, L.; Korganbayev, S.; De Landro, M.; Saccomandi, P. Thermomechanical Modeling of Laser Ablation Therapy of Tumors Sensitivity Analysis and Optimization of Influential Variables. *IEEE Trans. Biomed. Eng.* **2022**, *69*, 302–313. [CrossRef]
8. Namakshenas, P.; Di Matteo, F.M.; Bianchi, L.; Faiella, E.; Stigliano, S.; Quero, G.; Saccomandi, P. Optimization of laser dosimetry based on patient-specific anatomical models for the ablation of pancreatic ductal adenocarcinoma tumor. *Sci. Rep.* **2023**, *13*, 11053. [CrossRef]
9. Mohammazadeh, A.; Mahmouie, S.; Far, A.M. Monte Carlo and Bioheat Transfer Simulation of Dual Sequential Wavelength Laser for Port Wine Stains Treatment. In Proceedings of the 2020 28th Iranian Conference on Electrical Engineering (ICEE), Tabriz, Iran, 4–6 August 2020; Volume 20, pp. 7281–7296. [CrossRef]
10. Wang, X.; Qi, H.; Yang, X.; Xu, H. Analysis of the time-space fractional bioheat transfer equation for biological tissues during laser irradiation. *Int. J. Heat Mass Transf.* **2021**, *177*, 121555. [CrossRef]
11. Kishore, P.; Kumar, S.; Patel, V.M. Conjugate heat transfer analysis of laser-irradiated cylindrical-shaped biological tissue embedded with the optical inhomogeneity. *Int. J. Heat Mass Transf.* **2022**, *137*, 106302. [CrossRef]
12. Partovi, B.; Ahmadikia, H.; Mosharaf-Dehkordi, M. Analytical and numerical analysis of the dual-pulse lag heat transfer in a three-dimensional tissue subjected to a moving multi-point laser beam. *J. Therm. Biol.* **2023**, *112*, 103431. [CrossRef] [PubMed]
13. Hu, Y.; Zhang, X.-Y.; Li, X.-F. Thermoelastic analysis of biological tissue during hyperthermia treatment for moving laser heating using fractional dual-phase-lag bioheat conduction. *Int. J. Therm. Sci.* **2022**, *182*, 107806. [CrossRef]
14. Ma, J.; Yang, X.; Sun, Y.; Yang, J. Thermal damage in three-dimensional vivo bio-tissues induced by moving heat sources in laser therapy. *Sci. Rep.* **2019**, *9*, 10987. [CrossRef]
15. Bianchi, L.; Korganbayev, S.; Orrico, A.; De Landro, M.; Saccomandi, P. Quasi-distributed fiber optic sensor-based control system for interstitial laser ablation of tissue: Theoretical and experimental investigations. *Biomed. Opt. Express* **2021**, *12*, 2841–2858. [CrossRef] [PubMed]
16. Pham, N.T.; Lee, S.L.; Park, S.; Lee, Y.W.; Kang, H.W. Real-time temperature monitoring with fiber Bragg grating sensor during diffuser-assisted laser-induced interstitial thermotherapy. *J. Biomed. Opt.* **2017**, *22*, 45008. [CrossRef] [PubMed]
17. Singh, M.; Ma, R.; Zhu, L. Quantitative evaluation of effects of coupled temperature elevation, thermal damage, and enlarged porosity on nanoparticle migration in tumors during magnetic nanoparticle hyperthermia. *Int. Commun. Heat Mass Transf.* **2021**, *126*, 105393. [CrossRef]
18. Kosir, J.; Vella, D.; Lukac, M.; Jezersek, M. Towards personalized and versatile monitoring of temperature fields within heterogeneous tissues during laser therapies. *Biomed. Opt. Express* **2021**, *12*, 4530–4543. [CrossRef] [PubMed]
19. Singh, M.; Singh, T.; Soni, S. Pre-operative Assessment of Ablation Margins for Variable Blood Perfusion Metrics in a Magnetic Resonance Imaging Based Complex Breast Tumour Anatomy: Simulation Paradigms in Thermal Therapies. *Comput. Methods Programs Biomed.* **2021**, *198*, 105781. [CrossRef]
20. Pennes, H.H. Analysis of tissue and arterial blood temperatures in the resting human forearm. *J. Appl. Physiol.* **1948**, *1*, 93–112. [CrossRef]
21. Li, X.; Fan, S.; Zhao, Y.; Xiao, S. A numerical simulation of photothermal response in laser medicine. *Chin. Opt. Lett.* **2004**, *2*, 157–159.
22. Moritz, A.R.; Henriques, F.C. Studies of Thermal Injury: II. The Relative Importance of Time and Surface Temperature in the Causation of Cutaneous Burns. *Am. J. Pathol.* **1947**, *23*, 695–720. [CrossRef] [PubMed]
23. Henriques, F.; Montz, A.R. Studies of Thermal Injury: I. The Conduction of Heat to and through Skin and the Temperatures Attained Therein. A Theoretical and an Experimental Investigation. *Am. J. Pathol.* **1947**, *23*, 530–549. [PubMed]

24. Henriques, F. Studies of thermal injury; the predictability and the significance of thermally induced rate processes leading to irreversible epidermal injury. *Arch. Pathol.* **1947**, *43*, 489–502. [CrossRef]
25. Ishimaru, A. Diffusion of light in turbid material. *Appl. Opt.* **1989**, *28*, 2210–2215. [CrossRef] [PubMed]
26. Chen, Z.; Shi, J.; Yu, Y.; Chen, X. Photothermal and photoacoustic properties of biological tissues with micro tumors under the action of pulsed laser. *Optik* **2022**, *266*, 169637. [CrossRef]
27. Ye, Y. Experimental Research and Device Design of Laser-Induced Thermal Damage to Biological Tissues. Master's Thesis, South China University of Technology, Guangzhou, China, 2020.
28. Long, S.; Xu, Y.; Zhou, F.; Wang, B.; Zeng, Y. Temperature Simulation Model of Tumor Tissue in Tumor Bearing Mice during Photothermal Therapy. *Appl. Laser* **2018**, *38*, 142–149. [CrossRef]
29. Zhang, S.; Li, C.; Cao, L.; Moser, M.A.J.; Zhang, W.; Qian, Z.; Zhang, B. Modeling and ex vivo experimental validation of liver tissue carbonization with laser ablation. *Comput. Methods Programs Biomed.* **2022**, *217*, 106697. [CrossRef] [PubMed]
30. Rui, S.; Mi, Y.; Liu, L.; Yao, C.; Li, C. Study on temperature of liver and tumor under high frequency nanosecond pulsed field. In Proceedings of the 2015 IEEE Pulsed Power Conference (PPC), Austin, TX, USA, 31 May–4 June 2015; pp. 1–5.
31. Mi, Y.; Rui, S.; Li, C.; Yao, C.; Xu, J.; Bian, C.; Tang, X. Multi-parametric study of temperature and thermal damage of tumor exposed to high-frequency nanosecond-pulsed electric fields based on finite element simulation *Med. Biol. Eng. Comput.* **2017**, *55*, 1109–1122. [CrossRef] [PubMed]
32. Singh, M. Incorporating vascular-stasis based blood perfusion to evaluate the thermal signatures of cell-death using modified Arrhenius equation with regeneration of living tissues during nanoparticle-assisted thermal therapy. *Int. Commun. Heat Mass Transf.* **2022**, *135*, 106046. [CrossRef]
33. Singh, M.; Gu, Q.; Ma, R.; Zhu, L. Heating Protocol Design Affected by Nanoparticle Redistribution and Thermal Damage Model in Magnetic Nanoparticle Hyperthermia for Cancer Treatment. *J. Heat Transf.* **2020**, *142*, 072501. [CrossRef]
34. Ghasemi-Tabasi, H.; Jhabvala, J.; Boillat, E.; Ivas, T.; Drissi-Daoudi, R.; Logé, R.E. An effective rule for translating optimal selective laser melting processing parameters from one material to another. *Addit. Manuf.* **2020**, *36*, 101496. [CrossRef]
35. Hann, D.B.; Iammi, J.; Folkes, J. A simple methodology for predicting laser-weld properties from material and laser parameters. *J. Phys. D Appl. Phys.* **2011**, *44*, 445401. [CrossRef]

Disclaimer/Publisher's Note: The statements, opinions and data contained in all publications are solely those of the individual author(s) and contributor(s) and not of MDPI and/or the editor(s). MDPI and/or the editor(s) disclaim responsibility for any injury to people or property resulting from any ideas, methods, instructions or products referred to in the content.